




PAPER



Cite this: *Phys. Chem. Chem. Phys.*,
2021, **23**, 23953

Assembled triphenylamine *bis*-urea macrocycles: exploring photodriven electron transfer from host to guests†

Md Faizul Islam,  Ammon J. Sindt, Muhammad Saddam Hossain,
Pooja J. Ayare,  Mark D. Smith,  Aaron K. Vannucci, 
Sophya Garashchuk  and Linda S. Shimizu  *

Absorption of electronic acceptors in the accessible channels of an assembled triphenylamine (TPA) *bis*-urea macrocycle **1** enabled the study of electron transfer from the walls of the TPA framework to the encapsulated guests. The TPA host is isoskeletal in all host–guest structures analyzed with guests 2,1,3-benzothiadiazole, 2,5-dichlorobenzoquinone and I₂ loading in single-crystal-to-single-crystal transformations. Analysis of the crystal structures highlights how the spatial proximity and orientation of the TPA host and the entrapped guests influence their resulting photophysical properties and allow direct comparison of the different donor–acceptor complexes. Diffuse reflectance spectroscopy shows that upon complex formation **1**·2,5-dichlorobenzoquinone exhibits a charge transfer (CT) transition. Whereas, the **1**·2,1,3-benzothiadiazole complex undergoes a photoinduced electron transfer (PET) upon irradiation with 365 nm LEDs. The CT absorptions were also identified with the aid of time dependent density functional theory (TD-DFT) calculations. Cyclic voltammetry experiments show that 2,1,3-benzothiadiazole undergoes reversible reduction within the host–guest complex. Moreover, the optical band gaps of the host **1**·2,5-dichlorobenzoquinone (1.66 eV), and host **1**·2,1,3-benzothiadiazole (2.15 eV) complexes are significantly smaller as compared to the free host **1** material (3.19 eV). Overall, understanding this supramolecular electron transfer strategy should pave the way towards designing lower band gap inclusion complexes.

Received 1st July 2021,
Accepted 10th October 2021

DOI: 10.1039/d1cp03000k

rsc.li/pccp

Introduction

The rational design of photoactive molecules produced through electron transfer events is important and has applications for organic field effect transistors,¹ conductive materials,² sensors³ and electronic devices.⁴ This design includes thoughtful integration of suitable electron donors and acceptors through covalent or non-covalent interactions.^{5,6} In the covalent system, the electron transfer typically occurs by the participation of the orbitals of a bridging molecule *via* super-exchange interactions^{7,8} In comparison, electron transfer through non covalent interactions typically proceeds through the cross orbital interactions between the donor and acceptor molecules.⁷ Selection of an easily oxidizable donor and readily reduced

acceptor can promote the electron transfer event.⁹ Furthermore, suitable organization of the donor–acceptor molecules in closed space provides an optimum pathway for the electron transfer.¹⁰ Herein, we investigate how different acceptors encapsulated within an assembled triphenylamine (TPA) macrocycle framework promote electron transfer processes through space and modulate the photophysical properties (Fig. 1). The TPA macrocycle hosts are organized by ureas into columnar structures and load guests through single-crystal-to-single-crystal (SC–SC) guest exchange.¹¹ In particular, we examine if the electron transfer process is spontaneous or photo-triggered within these TPA supramolecular complexes based on reduction potential. After loading acceptors, the electron transfer can be triggered in the **1**·2,1,3-benzothiadiazole by irradiation with 365 nm UV LEDs.

Bottom-up approaches can build permanent porous crystalline materials with photoactive frameworks for applications such as gas separation, catalysis, photoreaction, and chemical sensing.^{12,13} This precise control provides materials with definite porosity and allows tunability of the chemical and physical properties.^{14,15} Encapsulation of suitable guests into such

Department of Chemistry and Biochemistry, University of South Carolina, Columbia South Carolina 29208, USA. E-mail: SHIMIZLS@mailbox.sc.edu

† Electronic supplementary information (ESI) available: Experimental details; synthesis and characterization; video of loading, SC-XRD data, absorbance emission, ¹H NMR, FTIR, Raman, CV, TD-DFT calculations. CCDC 2091812–2091814. For ESI and crystallographic data in CIF or other electronic format see DOI: 10.1039/d1cp03000k

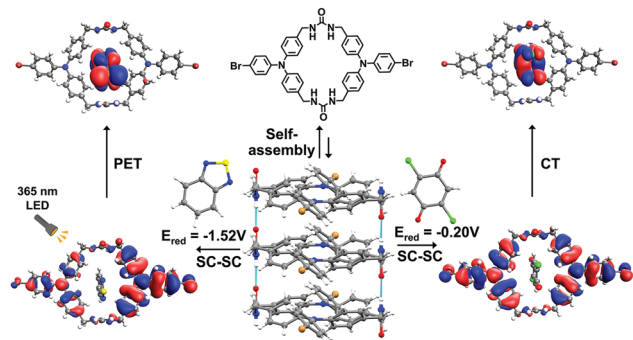


Fig. 1 Self-assembly of TPA macrocycles into columnar structure with encapsulated solvent. Heating the crystals generates empty channels that can undergo SC–SC transformations to load new guests. Upon illumination with 365 nm UV LEDs, photoinduced electron transfer occurs from the host to the acceptor bound inside the channel resulting in the formation of a charge separated state.

porous material can introduce intermolecular electron transfer events,^{16,17} that increase conductivity,^{18,19} initiate selective photocatalysis²⁰ and facilitate photooxidations.²¹ Triphenylamines (TPAs) are an excellent choice for donor molecules with an oxidizable central nitrogen atom and easily tunable frontier molecular orbital values.^{22,23} TPAs have extensive uses ranging from hole transporting materials in solar cells,²⁴ field effect transistors,²⁵ sensors²⁶ to smart fluorescent materials.²⁷ TPAs in conjugation with different acceptors can promote CT properties which eventually leads to lower band gap materials with higher conductive properties.^{28,29}

The Shimizu group employs urea guided assembly to organize TPAs into 1-dimensional columnar structures. The packing of these columns through urea–urea hydrogen bonding supported by π – π and halogen– π interactions gives microporous crystals.^{30,31} Prior work demonstrated that linear and macrocyclic brominated TPA dimers form stable radicals upon UV-irradiation in the solid state.^{32,33} From cyclic voltammetry measurements, the host **1** has oxidation potentials of 1.46 V and 1.86 V vs. Fc^+/Fc . The former oxidation potential is low enough to donate an electron to a variety of electron acceptors. For this study, we choose three different acceptors (2,1,3-benzothiadiazole,^{34,35} 2,5-dichloro-1,4-benzoquinone,^{36,37} and iodine^{38,39}) which were small enough to fit within the pores of the TPA framework and have shown promise in acting as electron acceptors for TPA complexes (Fig. 2). 2,1,3-Benzothiadiazole is one of the most commonly used acceptors with TPA due to its favorable reduction potential ($E_{\text{red}} = -1.12$ V vs. Fc^+/Fc).⁴⁰ It is typically covalently attached to TPA structures³⁵ or connected with a bridge to shift the fluorescence.⁴¹ Volatile iodine capture in porous materials has been intensively explored.^{42,43} Iodine ($E_{\text{red}} = -0.38$ V vs. Fc^+/Fc) can act as an electron acceptor which upon photoinduced electron transfer forms I_3^- or I_5^- .^{44,45} The third guest, a quinone derivative has been used in as an acceptor to trigger photoinduced electron transfer in TPAs.⁴⁶ The electron withdrawing chlorine in 2,5-dichloro-1,4-benzoquinone gives it a very favorable reduction potential ($E_{\text{red}} = 0.2$ V vs. Fc^+/Fc) and an

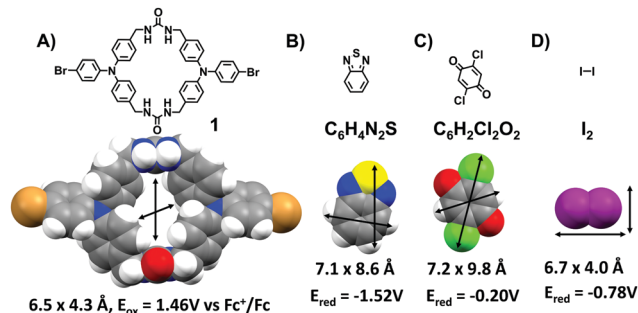


Fig. 2 Comparison of the pore size of the host to the size of the acceptors. (A) Host, **1**, $E_{\text{ox}} = 1.46$ V, (B) 2,1,3-Benzothiadiazole, (C) 2,5-dichloro-1,4-benzoquinone, (D) iodine. Host pore size is measured excluding van der Waals radii whereas acceptor sizes are determined including their van der Waals radii.

estimated $e(E_{\text{ox}}^{\text{D}+/ \text{D}} - E_{\text{red}}^{\text{A}/ \text{A}^-}) \sim 0.4065$, suggest the CT transition might be observed upon complex formation.⁴⁷

Here, 365 nm LEDs are used to provide external energy to trigger the transfer of electron from the host to the guest bound within the channel as this wavelength is near to the λ_{max} of the host. TD-DFT calculations were carried out to investigate the CT transition. In addition, electrochemical experiments were carried out in solid state to probe the redox wave of the host–guest complexes. Our goal is to probe how encapsulation of the acceptors inside the channels of the photoactive host triggers or modulates the photoinduced electron transfer and changes the functional properties of the host.

Experimental methods

Macrocycle **1** was synthesized in five steps according to the previous procedure (Scheme S1, ESI†).¹¹ Large colorless needle like crystals were obtained by the vapor diffusion of 1,2-dimethoxyethane (DME) in a DMSO solution of **1** (2.5 mg mL^{−1}).

Guest loading

Heating the **1**·DME crystals at 90 °C under vacuum facilitates removal of the DME in SC–SC guest exchange to give activated host **1**. Activated crystals of **1** (~10 mg) were exposed to the guest vapor of I_2 , 2,1,3-benzothiadiazole ($\text{C}_6\text{H}_4\text{N}_2\text{S}$) or 2,5-dichloro-1,4-benzoquinone ($\text{C}_6\text{H}_2\text{Cl}_2\text{O}_2$). For loading iodine, crystals of **1** were placed in a pre-weighed vial, pulled under vacuum (~0.001 torr) and then opened to an I_2 atmosphere. The other guests were heated to their sublimation temperature ($\text{C}_6\text{H}_4\text{N}_2\text{S}$ at 60 °C and $\text{C}_6\text{H}_2\text{Cl}_2\text{O}_2$ at 180 °C) in a sealed vessel under vacuum for ~24 h in presence of the activated host, resulting in formation of host–guest complexes *via* SC–SC transformations.¹¹

Physical measurements

Details of single crystal X-ray diffraction (SCXRD) analysis are provided in the ESI.† Solid state UV-Vis data was collected on PerkinElmer Lambda 35 spectrometer with UV vis software. Spectra were recorded from 330–800 nm at 1 nm steps at room

temperature. Photoluminescence data was collected on HORIBA Scientific Standard Microscope Spectroscopy Systems connected with iHR320 Spectrometer and Synchrony detector operating on Labspec 6 software. Spectra were recorded using 375 nm Laser excitation source power 0.1 mW with 10 \times UV objective. EPR experiments were carried out on a Bruker EMX plus equipped with a Bruker X-band microwave bridgehead and Xenon software (v 1.1b.66). Cyclic voltammetry measurements were carried out in dichloromethane using a WaveDriver 20 Bipotentiostat combined with Aftermath software. 0.1 M tetrabutylammonium hexafluorophosphate was used as the electrolyte. Measurements were performed in an H cell equipped with a SCE as reference, platinum wire as counter, and glassy carbon as working electrodes. To perform CV measurements in solid samples, a slurry was prepared by immersing the crystals in pentane. The slurry was then carefully deposited on the tip of the glassy carbon electrode. The crystals were then dried and used immediately for measurement. Measurements were performed at potential rate of 100 mV s⁻¹ and 50 mV s⁻¹.

Computations

To characterize the excited states of the host–guest complexes, time dependent density functional theory (TD-DFT) calculations were performed using Q-Chem.⁴⁸ The calculations were performed in gas phase using the single crystal XRD geometry of the complex. To lower the computational cost, all the calculations were carried out on 1 : 1 host–guest complexes using CAM-B3LYP⁴⁹ functional and basis set 6-31+G**,⁵⁰ which were shown to adequately describe systems characterized by CT.⁵¹

To assess the method dependence, calculations were also performed using LRC-wPBEh⁵²/6-31+G** method, which qualitatively yielded the same result. The electronic excitations were computed in the Random Phase Approximation (RPA) using 20 singlet states. The spectrum was generated by Gaussian broadening of the spectral lines using the standard deviation parameter σ set to 20 and 40 nm for 1-C₆H₄N₂S and 1-C₆H₂Cl₂O₂ respectively (ESI,† eqn (S1)).

Results and discussion

Structural comparison and iodine transport

The host **1** forms needle like crystals with the monoclinic space group *P*₂₁/*c* with disordered DME solvent encapsulated in a 2 : 1 host–guest ratio. The columnar structure of macrocycle **1** is primarily directed by three-centered urea hydrogen bonds ($d(\text{N}(\text{H})\cdots\text{O}) = 2.848(4)$ and $2.929(4)$ Å). Further π stacking of neighboring TPAs, stabilize the structure, which displays a macrocycle to macrocycle repeat distance of $4.620(2)$ Å. Individual columns pack into pseudo hexagonal rod packing array stabilized by halogen– π stacking interactions.¹¹

Once activated, host **1** is isoskeletal to the solvate, except the guest DME molecules are absent (Fig. 3).¹¹ The interior cross-section of the empty channel is $\sim 6.5 \times 4.3$ Å excluding the van der Waals radii of the participating atoms. The urea–urea hydrogen bonds in the empty framework are

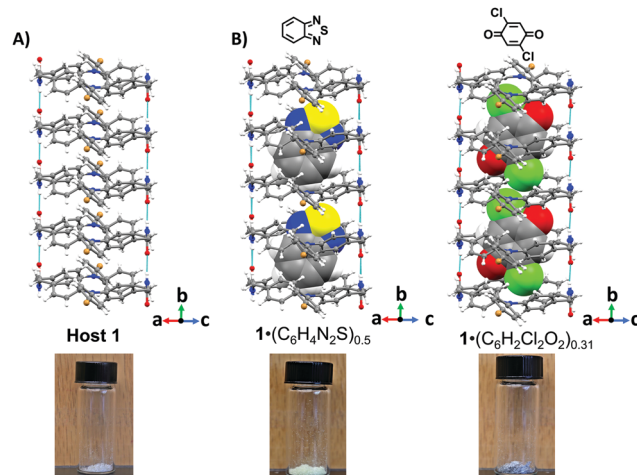


Fig. 3 Comparison of the 1-dimensional columnar structure from the activated host **1**¹¹ with two inclusion complexes containing electron acceptors. Disorder in the guests was omitted for clarity.

essentially unchanged, $\text{N}(\text{H})\cdots\text{O}$ $2.845(4)$ Å and $\text{N}(\text{H})\cdots\text{O}$ $2.914(4)$ Å.

During iodine loading (Fig. 4), a rapid visible color change occurred as the crystals are exposed to iodine vapor (Fig. 4B and see ESI,† for mp4 file). The change in weight of the crystals was measured over time to follow iodine absorption. The weight (wt) percent I₂ was calculated ($\text{wt. of I}_2 / (\text{wt. of } \mathbf{1} + \text{I}_2) \times 100\%$) and plotted *versus* time in Fig. 4A. Iodine appears to reach ~ 20 wt% occupancy in about 30 minutes, which corresponds to 2 : 1 host–guest ratio. Prolonged exposure up to 24 h resulted in the crystals turning black with a 30 wt% I₂ or a 1 : 1 host–guest ratio. Removal of the crystals from positive iodine atmosphere resulted in desorption of iodine from the channels over time.

To analyse the host–guest structure of the complex, freshly loaded crystals (with 30 min of iodine exposure) were removed from the I₂ atmosphere and analyzed using SC-XRD. The single crystal structure revealed that **1** retains the columnar

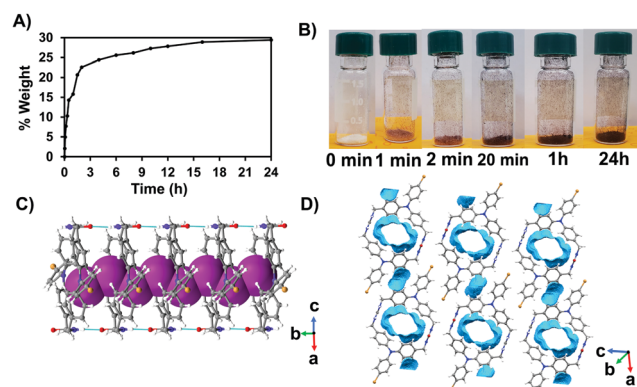


Fig. 4 Absorption of iodine by host **1**. (A) Calculated % weight change over time, (B) change in color of **1** over time of exposure to I₂. (C) Crystal structure of 1·I₂, (D) depiction of void space in host **1** (calculated by contact surface void space calculation using Mercury, Probe radius 0.9 Å, grid space 0.1 Å).

framework with disordered iodine arranged inside the channel in a zigzag pattern. However, the host-guest ratio was lower (1:0.34), suggesting the guest had partially desorbed prior to X-ray data collection. Though extensively disordered, the observed electron density in the channels is consistent with the diiodine molecules. Iodine can halogen bond with itself making polyiodide chains. The interatomic distances between each iodine peak are found to be I(1) 2.62 Å, I(2) 2.88, I(3) 2.98 Å, I(4) 2.79 Å, I(5) 2.88 Å which are close to the typical I-I distance in uncoordinated I₂ (Fig. 4C).⁵³ Previous studies on host **1** under pressurized Xe (9.5 bar at 298 K)¹¹ revealed two different adsorption sites for Xe, which likely correlate to the main channel and inter columnar pores highlighted in blue (Fig. 4D). The vdW radius of iodine (1.98 Å) is smaller than the vdW radius of Xe (2.16 Å). It is plausible that the higher host to iodine ratio after long equilibration times may be due to the adsorption of iodine in the inter columnar pores or deposition of iodine on the crystal surface.

The uptake of iodine was also explored from solution. Activated host **1** (8.5 mg) was soaked in a freshly prepared I₂ solution (0.5 mg mL⁻¹ cyclohexane). The concentration of I₂ in solution was monitored by recording the change in absorbance of the solution over time (Fig. S12 and S13, ESI†). Initially uptake of I₂ is rapid, reaching a 2:1 host-guest ratio in 2 h. After 2 days, the I₂ loading reaches saturation as the host-guest ratio reaches to 1:1 ratio with crystals turning black, similar to vapor loading experiments. The adsorbed I₂ can be removed by immersing the crystals in ethanol. The crystals changed their color from black, to brown, to colorless over time indicating that the adsorption of iodine is a reversible process (Fig. S17, ESI†). The absorption spectra of the ethanol solution were monitored overtime and plotted against the calibration curve to measure the amount of iodine released over time (Fig. S15 and S16, ESI†). After 36 h, 29 wt% of I₂ is released, which corresponds the complete removal of iodine from the crystals.

Two additional electron acceptors were loaded into host **1** by heating these guests to their sublimation temperature (C₆H₄N₂S at 60 °C and C₆H₂Cl₂O₂ at 180 °C) in a sealed vessel under vacuum for ~24 h in presence of the empty hosts. Guest loading did not change the crystal symmetry (monoclinic, *P*₂₁/*c*) but induced a color change with 1-C₆H₄N₂S and 1-C₆H₂Cl₂O₂ turning light yellow and slight grey respectively (Fig. 3B).¹¹ Fig. 3 compares the columnar structure of the activated host with the 1-C₆H₄N₂S and 1-C₆H₂Cl₂O₂. The guests are arranged in the channels in a planar tapelike fashion along the crystallographic *b* axis direction. In the complex 1-C₆H₄N₂S, the C₆H₄N₂S is disordered over two symmetry-equivalent sites per unit cell giving a host-guest ratio of 1:0.5. In 1-C₆H₂Cl₂O₂, the host to guest ratio refined to 1:0.31. Both the guests are aligned slightly tilted inside the channel. For 1-C₆H₄N₂S, the neighboring C-H... π distances are found to be around 4.01 Å and 4.17 Å (Fig. S10, ESI†) whereas for 1-C₆H₂Cl₂O₂ neighboring CH... π distances were found to be 3.81 Å and 4.05 Å (Fig. S11, ESI†). Additionally, the distance between the nitrogen of the C₆H₄N₂S and the neighboring urea of the host are found to be N...N 3.03 Å and N...C 2.878 Å (Fig. S10, ESI†), and the distance between the

carbonyl oxygen of the C₆H₂Cl₂O₂ and neighboring aromatic Hs are found to be 2.45 Å and 2.49 Å (Fig. S11, ESI†). These suggest that there is a possibility of host-guest interactions inside the channel but accurate metrics for these distances are obscured by the disorder.

Fourier Transform Infrared Spectroscopy (FT-IR) and Raman Spectroscopy showed that the crystals retain their characteristic properties upon guest loading. Both the complexes display similar signals for the host as well as new signals for the guests (Fig. S19, S20, S22 and S23, ESI†). For example, 1-C₆H₂Cl₂O₂ complex exhibits a new IR band at 1660 cm⁻¹ that corresponds to the carbonyl group in the quinone. The quinone carbonyl is also observed in the Raman spectra of 1-C₆H₂Cl₂O₂ complex at 1670 cm⁻¹. For the 1-C₆H₄N₂S complex, a slight enhancement of IR intensity around 755 cm⁻¹ is observed corresponding to C-N stretching. While in the Raman spectra, shows appearance of two new peaks at 1362, 1435 cm⁻¹ which corresponds to the aryl C-N stretching of the guest C₆H₄N₂S.

To characterize possible charge transfer (CT) in 1-I₂ complex, Raman spectra were taken to detect the iodide ion inside the host **1** as guest desorption complicated these studies. Raman spectra suggested that there is asymmetric I₃⁻ inside the channel before UV-irradiation. After 12 h of UV-irradiation, Raman shifts at 108 and 161 cm⁻¹ suggests that there is a possibility of forming linear I₅⁻ upon excitation (Fig. S18, ESI†).⁵⁴ X-ray Photoelectron Spectroscopy (XPS) studies of the complex after UV-irradiation also exhibited bands in the binding energy region of 620.1 eV, which corresponds to the ionic state of iodine (I₃⁻).⁵⁵ Again, these signals were weak (Fig. S21, ESI†), as one would expect for a complex which is only present in very minor amounts under the high vacuum conditions required for the XPS experiment. Therefore, we focused our efforts on characterizing the more stable 1-C₆H₄N₂S and 1-C₆H₂Cl₂O₂ complexes as they lack the guest desorption issues.

Photophysical measurements

Given the reduction potentials of the guests, we examined their potential CT by comparing their diffuse reflectance spectra before and after irradiating with 365 nm LEDs (Fig. 5). This wavelength was chosen as the host **1** has $\lambda_{\text{max}} = 366$ nm. Table 1 compare the diffuse reflectance spectrum of the complexes with the host and guests. Before UV-irradiation, 1-C₆H₄N₂S complex exhibits two absorption bands of similar intensity at $\lambda_{\text{max}} = 378$ and 399 nm (Fig. 5A). After irradiation, three intense absorptions bands are observed at $\lambda_{\text{max}} = 379$, 413 and 486 nm.

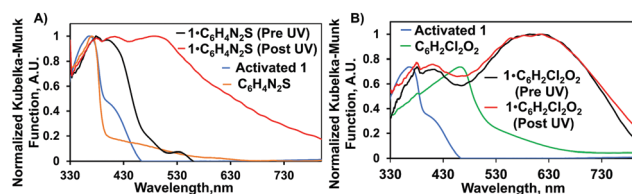


Fig. 5 Comparison of the diffuse reflectance spectra of activated host **1**, guests, and complexes before and after UV irradiation. (A) 1-C₆H₄N₂S and (B) 1-C₆H₂Cl₂O₂.

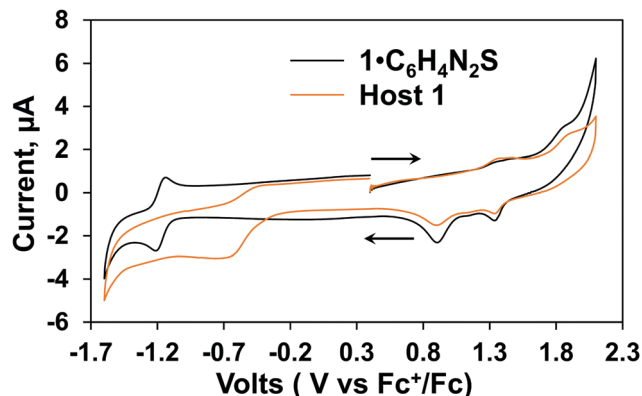
Table 1 Measured photophysical properties for different compounds in the solid state

Compound	λ_{abs} (nm)	λ_{ems} (nm) ($\lambda_{\text{exc}} = 375$ nm)
Activated 1	366	465
C ₆ H ₄ N ₂ S	370	
C ₆ H ₂ Cl ₂ O ₂	461	
1-C ₆ H ₄ N ₂ S (Pre UV)	378, 399	504
1-C ₆ H ₄ N ₂ S (Post UV)	379, 413, 486	500
1-C ₆ H ₂ Cl ₂ O ₂ (Pre UV)	381, 403, 594	468
1-C ₆ H ₂ Cl ₂ O ₂ (Post UV)	379, 411, 615	455

The long wavelength band is very broad and can be assigned as the CT state. The D'Souza group observed a CT state absorption band at $\lambda_{\text{max}} = 486$ nm for two TPA units with one benzothiadiazole unit.⁴⁰ The 1-C₆H₂Cl₂O₂, the pre-UV absorption spectra exhibits three bands at $\lambda_{\text{max}} = 381, 403$ and 594 nm with the later band attributed to a CT transition, suggesting that there is indeed CT in the complex prior to UV-exposure (Fig. 5B). After UV-irradiation, the spectra show similar three bands $\lambda_{\text{max}} = 379, 411$ and 615 nm. Photoluminescence spectra were recorded using 375 nm laser excitation. For both complexes, photoluminescence is significantly quenched (approximate 75–85%) after UV irradiation as expected for electron transfer upon excitation (Fig. S26 and S27, ESI†).⁵⁶

We measured the electron paramagnetic resonance (EPR) spectra of the crystalline host-guest complexes before and after UV-irradiation, as prior work suggests these conditions can induce radical formation in host 1 and its complexes.³³ Fig. S38 and S39 (ESI†) show both 1-C₆H₄N₂S and 1-C₆H₂Cl₂O₂ display EPR signals with broad axial powder pattern shapes and *g*-values of 2.007 after UV-irradiation. These EPR signals and *g*-values are similar to those reported by our group and others, suggesting that radicals are formed in the crystals under these conditions.^{33,57} Though low in quantity, the radicals persist after removing the complexes from the LEDs (Fig. S41, ESI†), suggesting that the reverse ET process is slow.

Cyclic voltammetry (CV) experiments were used to explore the redox behaviour of the complexes. The CV experiments were carried out with solid hosts adhered to the glassy carbon working electrode. A 0.1 M *n*-Bu₄N⁺PF₆[−] dichloromethane solution, a saturated calomel (SCE) reference electrode, and a Pt wire counter electrode were utilized. Fig. 6 compares the cyclic voltammogram of the host 1 and host-guest complex (1-C₆H₄N₂S) (Values of the potentials are converted from *vs.* SCE to *vs.* Fc^{+/}Fc).⁵⁸ Host 1 shows two oxidation events at 1.46 V and 1.86 V *vs.* Fc^{+/}Fc. In addition, host 1 has one irreversible reduction wave near −0.64 V, similar to the reduction potential of bromotriphenylamine.³³ In comparison, the host-guest complex exhibits two oxidation waves at 1.45 V and 1.81 V, similar to host 1. However, in the cathodic region, 1-C₆H₄N₂S does not exhibit a reduction event near −0.64 V, instead a reversible reduction wave at $E_{1/2} = -1.19$ V is observed. This reduction can be assigned to the reduction of the C₆H₄N₂S guest. Similar reduction profiles has been observed for benzothiadiazole covalently attached to TPA.⁵⁹ Unfortunately, the

**Fig. 6** Cyclic Voltammogram of Host 1 and 1-C₆H₄N₂S complex. (Potentials are converted to *vs.* Fc^{+/}Fc using $E_{\text{Fc}^+/\text{Fc}} = E_{\text{SCE}} + 0.4$ V⁵⁸).**Table 2** Electrochemical data and HOMO–LUMO energy gap of the host 1, 1-C₆H₄N₂S, 1-C₆H₂Cl₂O₂ complex

Compound	E_{ox} (V)	E_{red} (V)	HOMO (eV)	LUMO (eV)	Band gap, E_{GAP} (eV)
Host 1	1.46	−0.64	−6.26	−3.07	3.19
1-C ₆ H ₄ N ₂ S	1.45	−1.19	−6.25	−4.15	2.15
1-C ₆ H ₂ Cl ₂ O ₂	1.46	—	−6.26	−4.60	1.66

CV for 1-C₆H₂Cl₂O₂ was inconclusive due to difficulties in detecting the reduction wave of the loaded guest.

The redox potentials in conjunction with the diffuse reflectance spectra allowed us to calculate the HOMO and LUMO energies of the host and host-guest complexes using the following equations.⁶⁰

$$E_{\text{HOMO}} = -4.8 \text{ eV} - V_{\text{ox}}$$

$$E_{\text{LUMO}} = E_{\text{HOMO}} + E_{\text{GAP}}$$

where, −4.8 eV is the oxidation potential of ferrocene from vacuum, V_{ox} is the onset potential for the oxidation of the complexes *versus* Fc^{+/}Fc and E_{GAP} is the absorption edge energy from the diffuse reflectance spectra (Fig. S36 and S37, ESI†). The obtained results are listed in Table 2. The HOMO values for the host and host-guest complexes remain almost the same. Upon guest complexation, the optical band gap, E_{GAP} of the materials becomes significantly reduced. The band gap of 1-C₆H₂Cl₂O₂ (1.66 eV) is lower than the band gap of 1-C₆H₄N₂S (2.15 eV) which is due to the better electron withdrawing capacity of the C₆H₂Cl₂O₂ guest.

Analysis of the electronic excitations

The electronic structures of the host, guest and host-guest complexes are obtained from the TD-DFT calculations using the experimental geometry on a truncated model comprised of one macrocycle and one guest (about 100 atoms) due to practical considerations. Fig. 7 compares the frontier molecular orbitals, their corresponding energies and the HOMO–LUMO gap for the host, guests, and host-guest complexes. Examination

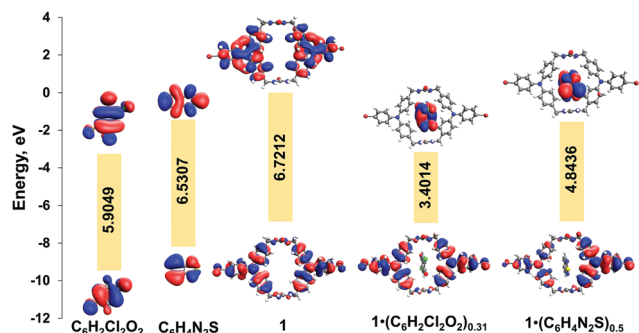


Fig. 7 Frontier molecular orbitals and calculated HOMO–LUMO levels of the host, guests, and host–guest complexes.

of the frontier orbitals of host **1**, shows that the electron density is delocalized over the whole molecule in the HOMO, while in the LUMO, the density is delocalized over the phenyl rings. Host **1** has a HOMO–LUMO gap of 6.72 eV. In both host–guest complexes, while the HOMO is distributed over the electron donor host **1**, the LUMO is solely localized on the guest molecule, suggesting a movement of electron from the host donor to the guest acceptor, resulting in the formation of charge separated states. Also, the HOMO–LUMO gap is significantly reduced upon the inclusion of guests, in agreement with the optical and electrochemical results. Similar to the optical band gap results, $\text{C}_6\text{H}_2\text{Cl}_2\text{O}_2$ guest exhibits larger HOMO–LUMO gap reduction compared to the guest $\text{C}_6\text{H}_4\text{N}_2\text{S}$. Upon inclusion of $\text{C}_6\text{H}_4\text{N}_2\text{S}$, the HOMO–LUMO gap is reduced to 4.84 eV whereas inclusion of $\text{C}_6\text{H}_2\text{Cl}_2\text{O}_2$ results in a reduced HOMO–LUMO gap of 3.40 eV.

Next, to gage the accuracy of the calculations, we computed the UV/Vis spectra for both host–guest complexes and compared with the experimental diffuse reflectance spectra. Theoretical UV/Vis spectra were obtained from the TD-DFT excitation energies computed within the RPA for the molecular model of a single host–guest unit of about 100 atoms due to practical constraints (ESI† eqn (S1)). The energy gaps computed in truncated models of a solid such as ours, are known to be overestimated. We have verified this trend by computing the HOMO–LUMO gaps for the host represented by one, two and three macrocycles at experimental geometry. The respective gaps are 7.07, 6.77 and 6.69 eV, which shows a reduction when going from one to three macrocycles, by a factor 0.946. This provides a justification for multiplying the calculated spectra of host–guest complexes by a factor of 0.845 and 0.927 for the $1\cdot\text{C}_6\text{H}_4\text{N}_2\text{S}$ and $1\cdot\text{C}_6\text{H}_2\text{Cl}_2\text{O}_2$ respectively (Tables S7 and S8, ESI†). These factors were chosen to best fit the computed spectra with the experimental spectra (Fig. 8). After scaling, the calculated spectra of $1\cdot\text{C}_6\text{H}_4\text{N}_2\text{S}$ matches qualitatively with the higher energy transitions of the experimental diffuse reflectance spectra (Fig. 8A), although it missed the transition at 530 nm. Fig. 8B compares the simulated UV/Vis and experimental diffuse reflectance spectra of $1\cdot\text{C}_6\text{H}_2\text{Cl}_2\text{O}_2$ and provides a qualitative match with the spectral features.

Next, the Natural Transition Orbitals (NTOs)⁶¹ were generated for transitions with high oscillator strength. Fig. 8B compares the highest occupied natural transition orbitals (HONTO) and the lowest unoccupied natural transition orbitals (LUNTO)

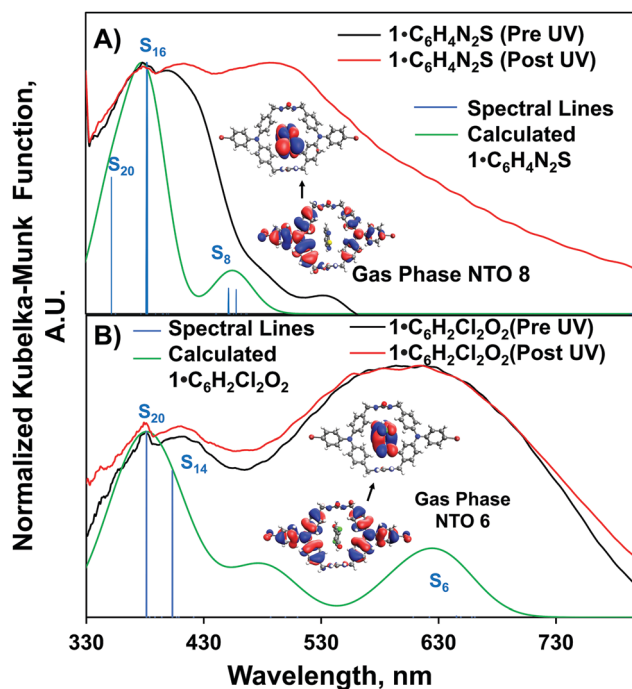


Fig. 8 Comparison of the experimental diffuse reflectance spectra with TD-DFT calculated spectra including corresponding spectral lines, HONTO and LUNTO of the charge transfer transition for (A) $1\cdot\text{C}_6\text{H}_4\text{N}_2\text{S}$ and (B) $1\cdot\text{C}_6\text{H}_2\text{Cl}_2\text{O}_2$.

for the transition corresponding to electron transfer event. (see ESI† for additional NTOs). For $1\cdot\text{C}_6\text{H}_4\text{N}_2\text{S}$ complex, the transition at S_{20} involves the $\pi\pi^*$ transition of the host molecule, S_{16} has some CT $\pi\pi^*$ (Fig. S48, ESI†) transition while the low energy transition at S_8 has the direct transition from the HOMO of the host to the LUMO of the guest (Fig. 8B). So, we can assign the band corresponding this transition as the CT transition band. For $1\cdot\text{C}_6\text{H}_2\text{Cl}_2\text{O}_2$ complex, S_{20} and S_{14} has some host **1** to guest character (Fig. S49, ESI†), while the low energy state S_6 shows the direct transition from the HOMO of host **1** to the LUMO of the guest. Therefore, this low energy band was assigned as the direct CT transition band for the complex.

We have also analyzed the charge transfer characteristics of the complexes based on the dipole moment in Debye (μ) and linear electron–hole (e/h) distance in angstrom (\AA) encoded in the transition density matrix analysis to probe the charge transfer (Table S9, ESI†). Large electron–hole separation and dipole moment are associated with the CT character. For example, for $1\cdot\text{C}_6\text{H}_4\text{N}_2\text{S}$ the dipole moment of the states S_8 , S_{16} are S_{20} are 15.83, 7.14 and 1.99 Debye respectively, while the total molecular dipole is 1.62 Debye; the electron–hole distances for the same states are 3.23, 1.12 and 0.35 \AA . Thus, S_8 and S_{16} are characterized as the CT states, while S_{20} is not.

Conclusions

In summary, three guests with reasonable reduction potentials with respect to TPA were successfully loaded in the porous

organic crystals of triphenylamine *bis*-urea macrocycles. Comparison of the crystal structures demonstrated that the columnar framework was isostructural in the host-guest complexes with the guests exhibiting some disorder within the channels. Iodine loaded reversibly into the channels from both solution and vapor and exhibited XPS and Raman bands indicative of CT state formation upon UV-irradiation. However, the slow desorption of I₂ under ambient conditions complicated these studies.

2,5-Dichloro-1,4-benzoquinone, gave a crystalline complex, 1-C₆H₂Cl₂O₂ which likely formed CT transition under ambient conditions. Indeed, having lower reduction potential of the acceptor facilitates the lowering of the energy requirement for photoinduced electron transfer estimated $e(E_{\text{ox}}^{\text{D+D}} - E_{\text{red}}^{\text{A/A-}}) \sim 0.4065$. TD-DFT computations using CAM-B3LYP functional and basis set 6-31+G** were able to qualitatively predict experimental properties in this complex including the intense long wavelength band, which is present upon complex formation. The absorption bands at 379, 411 and 615 nm all have host to guest CT character with the higher wavelength band exhibiting direct HOMO to LUMO character. Finally, analysis of FMO suggests that inclusion of C₆H₂Cl₂O₂ affords the lowest HOMO-LUMO gap between the complexes.

In comparison, 2,1,3-benzothiadiazole proved to be a guest with an intermediate reduction potential, which enabled us to study photoinduced electron transfer upon UV-irradiation. This crystalline 1-C₆H₄N₂S complex has an estimated $e(E_{\text{ox}}^{\text{D+D}} - E_{\text{red}}^{\text{A/A-}}) \sim 1.49$ and required UV-irradiation to form the CT state forming an intense visible broad new band at 486 nm. The complex shows a reversible reduction wave at $E_{1/2} = -1.6$ V for the acceptor, which has been observed in covalent donor-acceptor TPA systems. Future work will focus on measurement of conductivity in these supramolecular complexes. Overall, we demonstrate that supramolecular strategies are an effective and easy method to post-modify porous organic crystals by CT between host and guest and may be applicable to developing better electroactive materials.

Author contributions

LSS initiated studies. SG, MSH, MFI, LSS, AJS, AKV planned experiments, analyzed data and wrote the manuscript. PJA, SG, MSH, MFI, AJS performed experiments and/or calculations.

Conflicts of interest

There are no conflicts to declare.

Acknowledgements

This work was supported in part by the National Science Foundation CHE-1904386. The computational work (S. G.) is based upon work supported in part by the NSF and SCEPSCoR/IDEA

Program under Grants No. CHE-1955768 and GEAR CRP 20-GC03, respectively.

References

- 1 C. Zhang, P. Chen and W. Hu, *Chem. Soc. Rev.*, 2015, **44**, 2087–2107.
- 2 S. Logothetidis, *Mater. Sci. Eng. B Solid-State Mater. Adv. Technol.*, 2008, **152**, 96–104.
- 3 J. T. Mabeck and G. G. Malliaras, *Anal. Bioanal. Chem.*, 2006, **384**, 343–353.
- 4 N. Koch, *ChemPhysChem*, 2007, **8**, 1438–1455.
- 5 M. Natali, S. Campagna and F. Scandola, *Chem. Soc. Rev.*, 2014, **43**, 4005–4018.
- 6 C. B. Larsen and O. S. Wenger, *Angew. Chem., Int. Ed.*, 2018, **57**, 841–845.
- 7 M. R. Wasielewski, *Chem. Rev.*, 1992, **92**, 435–461.
- 8 S. V. Rosokha and J. K. Kochi, *Acc. Chem. Res.*, 2008, **41**, 641–653.
- 9 M. D. Newton, *Chem. Rev.*, 1991, **91**, 767–792.
- 10 K. A. Jolliffe, T. D. M. Bell, K. P. Ghiggino, S. J. Langford and M. N. Paddon-row, *Angew. Chem., Int. Ed.*, 1998, **37**, 915–919.
- 11 A. J. Sindt, M. D. Smith, S. Berens, S. Vasenkov, C. R. Bowers and L. S. Shimizu, *Chem. Commun.*, 2019, **55**, 5619–5622.
- 12 M. E. Davis, *Nature*, 2002, **417**, 813–821.
- 13 E. Mattia and S. Otto, *Nat. Nanotechnol.*, 2015, **10**, 111–119.
- 14 A. G. Slater and A. I. Cooper, *Science*, 2015, **348**, aaa8075.
- 15 Z. Meng, R. M. Stolz and K. A. Mirica, *J. Am. Chem. Soc.*, 2019, **141**, 11929–11937.
- 16 Y. Jin, Q. Zhang, Y. Zhang and C. Duan, *Chem. Soc. Rev.*, 2020, **49**, 5561–5600.
- 17 S. Yamamoto, J. Pirillo, Y. Hijikata, Z. Zhang and K. Awaga, *Chem. Sci.*, 2018, **9**, 3282–3289.
- 18 A. A. Talin, A. Centrone, A. C. Ford, M. E. Foster, V. Stavila, P. Haney, R. A. Kinney, V. Szalai, F. El Gabaly, H. P. Yoon, F. Léonard and M. D. Allendorf, *Science*, 2014, **343**, 66–69.
- 19 C. W. Kung, K. Otake, C. T. Buru, S. Goswami, Y. Cui, J. T. Hupp, A. M. Spokoiny and O. K. Farha, *J. Am. Chem. Soc.*, 2018, **140**, 3871–3875.
- 20 T. Uchikura, M. Oshima, M. Kawasaki, K. Takahashi and N. Iwasawa, *Angew. Chem., Int. Ed.*, 2020, **59**, 7403–7408.
- 21 Y. Furutani, H. Kandori, M. Kawano, K. Nakabayashi, M. Yoshizawa and M. Fujita, *J. Am. Chem. Soc.*, 2009, **131**, 4764–4768.
- 22 J. Wang, K. Liu, L. Ma and X. Zhan, *Chem. Rev.*, 2016, **116**, 14675–14725.
- 23 Y. Shiota, *J. Mater. Chem.*, 2005, **15**, 75–93.
- 24 P. Agarwala and D. Kabra, *J. Mater. Chem. A*, 2017, **5**, 1348–1373.
- 25 Y. Song, C. Di, X. Yang, S. Li, W. Xu, Y. Liu, L. Yang, Z. Shuai, D. Zhang and D. Zhu, *J. Am. Chem. Soc.*, 2006, **128**, 15940–15941.
- 26 A. Chowdhury and P. S. Mukherjee, *J. Org. Chem.*, 2015, **80**, 4064–4075.
- 27 P. Xue, P. Chen, J. Jia, Q. Xu, J. Sun, B. Yao, Z. Zhang and R. Lu, *Chem. Commun.*, 2014, **50**, 2569–2571.
- 28 S. Zeng, L. Yin, C. Ji, X. Jiang, K. Li, Y. Li and Y. Wang, *Chem. Commun.*, 2012, **48**, 10627–10629.

- 29 J. Preat, C. Michaux, D. Jacquemin and E. A. Perpète, *J. Phys. Chem. C*, 2009, **113**, 16821–16833.
- 30 L. S. Shimizu, S. R. Salpage and A. A. Korous, *Acc. Chem. Res.*, 2014, **47**, 2116–2127.
- 31 B. A. Dehaven, D. W. Goodlett, A. J. Sindt, N. Noll, M. De Vetta, M. D. Smith, C. R. Martin, L. González and L. S. Shimizu, *J. Am. Chem. Soc.*, 2018, **140**, 13064–13070.
- 32 A. J. Sindt, B. A. Dehaven, D. F. McEachern, D. M. M. M. Dissanayake, M. D. Smith, A. K. Vannucci and L. S. Shimizu, *Chem. Sci.*, 2019, **10**, 2670–2677.
- 33 A. J. Sindt, B. A. Dehaven, D. W. Goodlett, J. O. Hartel, P. J. Ayare, Y. Du, M. D. Smith, A. K. Mehta, A. M. Brugh, M. D. E. Forbes, C. R. Bowers, A. K. Vannucci and L. S. Shimizu, *J. Am. Chem. Soc.*, 2020, **142**, 502–511.
- 34 T. Suzuki, T. Tsuji, T. Okubo, A. Okada, Y. Obana, T. Fukushima, T. Miyashi and Y. Yamashita, *J. Org. Chem.*, 2001, **66**, 8954–8960.
- 35 C. B. Larsen, H. Van Der Salm, G. E. Shillito, N. T. Lucas and K. C. Gordon, *Inorg. Chem.*, 2016, **55**, 8446–8458.
- 36 V. R. Hathwar, R. G. Gonnade, P. Munshi, M. M. Bhadbhade and T. N. G. Row, *Cryst. Growth Des.*, 2011, **11**, 1855–1862.
- 37 M. T. Huynh, C. W. Anson, A. C. Cavell, S. S. Stahl and S. Hammes-Schiffer, *J. Am. Chem. Soc.*, 2016, **138**, 15903–15910.
- 38 W. Borley, B. Watson, Y. P. Nizhnik, M. Zeller and S. V. Rosokha, *J. Phys. Chem. A*, 2019, **123**, 7113–7123.
- 39 C. L. Bentley, A. M. Bond, A. F. Hollenkamp, P. J. Mahon and J. Zhang, *J. Phys. Chem. C*, 2015, **119**, 22392–22403.
- 40 Y. Rout, Y. Jang, H. B. Gobeze, R. Misra and F. D'souza, *J. Phys. Chem. C*, 2019, **123**, 23382–23389.
- 41 S. I. Kato, T. Matsumoto, M. Shigeiwa, H. Gorohmaru, S. Maeda, T. Ishi-i and S. Mataka, *Chem. – Eur. J.*, 2006, **12**, 2303–2317.
- 42 W. Xie, D. Cui, S. R. Zhang, Y. H. Xu and D. L. Jiang, *Mater. Horiz.*, 2019, **6**, 1571–1595.
- 43 R. X. Yao, X. Cui, X. X. Jia, F. Q. Zhang and X. M. Zhang, *Inorg. Chem.*, 2016, **55**, 9270–9275.
- 44 P. H. Svensson and L. Kloo, *Chem. Rev.*, 2003, **103**, 1649–1684.
- 45 T. Hasell, M. Schmidtman and A. I. Cooper, *J. Am. Chem. Soc.*, 2011, **133**, 14920–14923.
- 46 X. Y. Liu, Y. T. Long and H. Tian, *RSC Adv.*, 2015, **5**, 57263–57266.
- 47 S. Kepler, M. Zeller and S. V. Rosokha, *J. Am. Chem. Soc.*, 2019, **141**, 9338–9348.
- 48 Y. Shao, *et. al.*, *Mol. Phys.*, 2015, **113**, 184–215.
- 49 T. Yanai, D. P. Tew and N. C. Handy, *Chem. Phys. Lett.*, 2004, **393**, 51–57.
- 50 R. Ditchfield, W. J. Hehre and J. A. Pople, *J. Chem. Phys.*, 1971, **54**, 720–723.
- 51 C. Bernini, L. Zani, M. Calamante, G. Reginato, A. Mordini, M. Taddei, R. Basosi and A. Sinicropi, *J. Chem. Theory Comput.*, 2014, **10**, 3925–3933.
- 52 M. A. Rohrdanz, K. M. Martins and J. M. Herbert, *J. Chem. Phys.*, 2009, **130**, 054112.
- 53 C. R. Groom, I. J. Bruno, M. P. Lightfoot and S. C. Ward, *Acta Crystallogr., Sect. B: Struct. Sci., Cryst. Eng. Mater.*, 2016, **72**, 171–179.
- 54 L. Alvarez, J. L. Bantignies, R. Le Parc, R. Aznar, J. L. Sauvajol, A. Merlen, D. MacHon and A. San Miguel, *Phys. Rev. B: Condens. Matter Mater. Phys.*, 2010, **82**, 1–7.
- 55 C. Pei, T. Ben, S. Xu and S. Qiu, *J. Mater. Chem. A*, 2014, **2**, 7179–7187.
- 56 S. Doose, H. Neuweiler and M. Sauer, *ChemPhysChem*, 2009, **10**, 1389–1398.
- 57 Y. Mu, Y. Liu, H. Tian, D. Ou, L. Gong, J. Zhao, Y. Zhang, Y. Huo, Z. Yang and Z. Chi, *Angew. Chem., Int. Ed.*, 2021, **60**, 6367–6371.
- 58 D. M. Peloquin, D. R. Dewitt, S. S. Patel, J. W. Merkert, B. T. Donovan-Merkert and T. A. Schmedake, *Dalton Trans.*, 2015, **44**, 18723–18726.
- 59 J. E. Barnsley, G. E. Shillito, C. B. Larsen, H. Van Der Salm, L. E. Wang, N. T. Lucas and K. C. Gordon, *J. Phys. Chem. A*, 2016, **120**, 1853–1866.
- 60 L. V. Brownell, K. A. Robins, Y. Jeong, Y. Lee and D. C. Lee, *J. Phys. Chem. C*, 2013, **117**, 25236–25247.
- 61 R. L. Martin, *J. Chem. Phys.*, 2003, **118**, 4775–4777.